Journal of Catalysis 349 (2017) 175–182

Contents lists available at ScienceDirect

Journal of Catalysis

journal homepage: www.elsevier.com/locate/jcat

Formation of $NiCo_2O_4$ rods over Co_3O_4 nanosheets as efficient catalyst for Li–O_2 batteries and water splitting

Palanichamy Sennu [a], Hyo Seok Park [c], Kwang Uk Park [d], Vanchiappan Aravindan [e], Kee Suk Nahm [b,c,d], Yun-Sung Lee [a,*]

[a] Faculty of Applied Chemical Engineering, Chonnam National University, Gwang-ju 500-757, Republic of Korea
[b] R&D Education Centre for Fuel Cell Materials & Systems, Chonbuk National University, Jeonju 561-756, Republic of Korea
[c] Department of Energy Storage and Conversion Engineering, Chonbuk National University, Jeonju 561-756, Republic of Korea
[d] School of Engineering, Chonbuk National University, Jeonju 561-756, Republic of Korea
[e] Energy Research Institute @ NTU (ERI@N), Nanyang Technological University, Research Techno Plaza, 50 Nanyang Drive, Singapore 637553, Singapore

ARTICLE INFO

Article history:
Received 16 November 2016
Revised 3 March 2017
Accepted 19 March 2017
Available online 5 April 2017

Keywords:
Lithium–Oxygen battery
Bifunctional catalyst
Oxygen evolution
Oxygen reduction

ABSTRACT

A 3D structured $NiCo_2O_4$@Co_3O_4 hybrid was prepared by a two-step hydrothermal approach and subsequently employed as a highly efficient catalyst in oxygen reduction reactions (ORRs)/oxygen evolution reactions (OERs) and from a Li–O_2 battery perspective. The Co-NC possesses interconnected $NiCo_2O_4$ nanorods grown over a Co_3O_4 nanosheet structure, which facilitates charge transfer and enhances the electrical conductivity. Moreover, the 3D structured hybrids are directly used as a cathode catalyst for the Li–O_2 system and displayed a maximum in-depth-specific discharge capacity of 4386 mA h g^{-1}. In addition, significantly improved and stable cycling performance up to 60 cycles is observed compared with Co_3O_4 nanosheets at the limited capacity range of 500 mA h g^{-1}. The excellent electrochemical performance of the $NiCo_2O_4$@Co_3O_4 hybrid is mainly associated with the oxygen-deficient 3D architecture providing more catalytic active sites and can accommodate more discharge products. Further, ORR/OER activities of $NiCo_2O_4$@Co_3O_4 hybrid in aqueous media are also evaluated in 0.1 M KOH solution using the rotating ring disk electrode technique. For instance, the OER activity of $NiCo_2O_4$@Co_3O_4 hybrid (apex current is 4.18 mA cm^{-2}) is an approximately 2.25 times higher than that of commercial RuO_2 catalyst (1.84 mA cm^{-2}). Since the catalytic activity in aqueous and organic medium is not necessarily the same, but of $NiCo_2O_4$@Co_3O_4 hybrid exhibiting excellent ORR/OER characteristics in both cases is worth mentioning.

1. Introduction

The development of energy conversion and storage systems from sustainable renewable sources is a major concern for this modern society due to global warming by CO_2 emissions and the depletion of fossil fuels. In recent years, metal–air batteries and hydrogen-based fuel cells have received considerable attention and can be used as the most promising sources for future electric vehicles (EVs) rather than the existing intermittence systems such as lead–acid and Li-ion batteries [1–4]. Oxygen reduction reactions (ORRs) and oxygen evolution reactions (OERs) are fundamental in metal–air batteries and H_2 production from photoelectrochemical water splitting. The Li–O_2 cell has received significant attention because of its high specific energy, low weight, and safety. The theoretical specific energies of Li-O_2 systems vary from ~3500 to 5200 W h kg^{-1} on the basis of the cathode materials and electrolytes (aqueous, non-aqueous, solid-state, or hybrid form) [4–7]. Abraham et al. [8] first reported the rechargeability of a Li–O_2 cell, and the specific capacity is limited by ~1600 mA h g^{-1} because the intrinsic cell chemistry in the porous carbon cathode provides a low energy and power ability. However, the major technical difficulties in Li–O_2 batteries are the slow kinetics of Li_2O_2 formation and decomposition on the electrode surface, the high rate capability, the large polarization, and the efficiency, which limit practical applications. However, an efficient catalyst can accelerate the performance of Li-O_2 batteries in terms of reversibility and suppressing the over-potential [9,10]. In some cases, the carbon electrode and some of the residual solids (e.g. Li_2O_2) act as promoter to improve the battery performance [11]. In 2006, Bruce et al. [12] successfully demonstrated the importance of the catalyst for improving the electrochemical activity. Pt, Au, Ir,

* Corresponding author.
E-mail address: leeys@chonnam.ac.kr (Y.-S. Lee).

http://dx.doi.org/10.1016/j.jcat.2017.03.015
0021-9517/

RuO_2, and their composites with carbonaceous materials have shown excellent bifunctional (ORR/OER) activities but still suffered owing to their expense and low abundance [13–17]. Further, carbonaceous materials are also to be used as bifunctional catalyst, but the reversibility and over-potential of Li-O_2 cell remain an issue. Hence, the search for an alternate catalyst to Li-O_2 systems is desperately required without compromising performance. Transition-metal oxides or chalcogenides containing Co, Mn, and Ni have been demonstrated to be effective bifunctional electrocatalysts for Li-O_2 batteries [18–23]. Zhao et al. [19] proposed free-standing Co_3O_4 hollow flakes grown on Ni-foam as catalyst and the cell displayed a capacity of 2460 mA h g^{-1} with improved stability up to 35 cycles. Interestingly the usage of ordered mesoporous $NiCo_2O_4$ catalyst enhanced the specific capacity (4120 mA h g^{-1}) and discharged voltage plateau of a Li–O_2 battery compared to Ketjen black (KB) based cell [24]. The electrical conductivity and electrochemical property of $NiCo_2O_4$ are at least two orders of magnitude higher than the monometallic NiO and Co_3O_4 materials [25–27]. Recent studies have shown that the morphology and dimensional features of a catalyst heighten the reaction kinetics and reduce the over-potential with a long-term cycle stability. Overall, the controlled arrangement of facets and surface structures is needed to reduce the energy barriers between the oxidation and reduction processes [28–37]. Apparently, the catalytic activity of a catalyst in aqueous and organic medium is entirely different process and its reaction mechanism as well. This means, a best catalyst in the aqueous media is not necessary to exhibit similar characteristics in organic solution or vice versa. However, in some exceptional cases, better catalytic activity in both cases is reported. Since the ORR/OER activity in the aqueous media will be certainly useful for the development of catalyst for aqueous and hybrid Li-O_2 batteries, and Zn-O_2 system. Also, a prominent application of water splitting is worth mentioning.

Here, we report the fabrication of a 3D $NiCo_2O_4$@Co_3O_4 (Co-NC) catalyst from Co_3O_4 nanosheets (Co_3O_4-NS) using a two-step hydrothermal approach. Its bifunctional electro-catalytic activities were explored in both aqueous and non-aqueous solutions (Scheme 1). The presence of $NiCo_2O_4$ nanorods ($NiCo_2O_4$-NR) over the Co_3O_4-NS creates enlarged voids, which can increase the accessibility and diffusion capability of Li^+ ions and O_2 in the Li-O_2 battery. Furthermore, the $NiCo_2O_4$-NR influences the charge transfer capability and the electrical properties between the Co_3O_4-NS and the Co-NC/Li_2O_2 interface.

2. Experimental section

2.1. Preparation of Co-NC

The Co-NC catalyst was synthesized from 2D Co_3O_4-NS using a two-step hydrothermal method. First, the starting material Co_3O_4-NS was obtained according to our previous report [38]. Subsequently, the $NiCo_2O_4$-NR were grown in the second step. Briefly, 0.290 mg of $Ni(NO_3)_2{\cdot}H_2O$ (Junsei, Japan), 0.582 mg of $Co(NO_3)_2{\cdot}H_2O$ (Junsei, Japan), and 1.8 g of urea were dissolved in 100 mL of water. Then, the desired amount of Co_3O_4-NS (800 mg) was added to the above solution under continuous stirring. After 10 min, the mixture was transferred to a 120 mL Teflon-lined rotation autoclave (homemade, 10–300 rpm) and then heated at 160 °C for 2 h. The resultant black–brown product was repeatedly washed with water and ethanol. Finally, the sample pyrolyzed at 300 °C for 4 h in an air atmosphere to obtain the hybrid Co-NC catalyst.

2.2. Physical characterization

Powder X-ray diffractometer (XRD, Rint 1000, Rigaku, Japan) equipped with Cu Kα radiation was used to study the structural properties. BET surface area measurements were conducted using a Micromeritics ASAP 2010 surface area analyzer. Surface morphological features of the samples were recorded using a field-emission scanning electron microscope (FE-SEM, S4700, Hitachi, Japan). X-ray photoelectron spectroscopy (XPS) was performed using a spectrometer (Multilab 2000, UK) with monochromatic Al Kα radiation ($h\nu$ = 1486.6 eV).

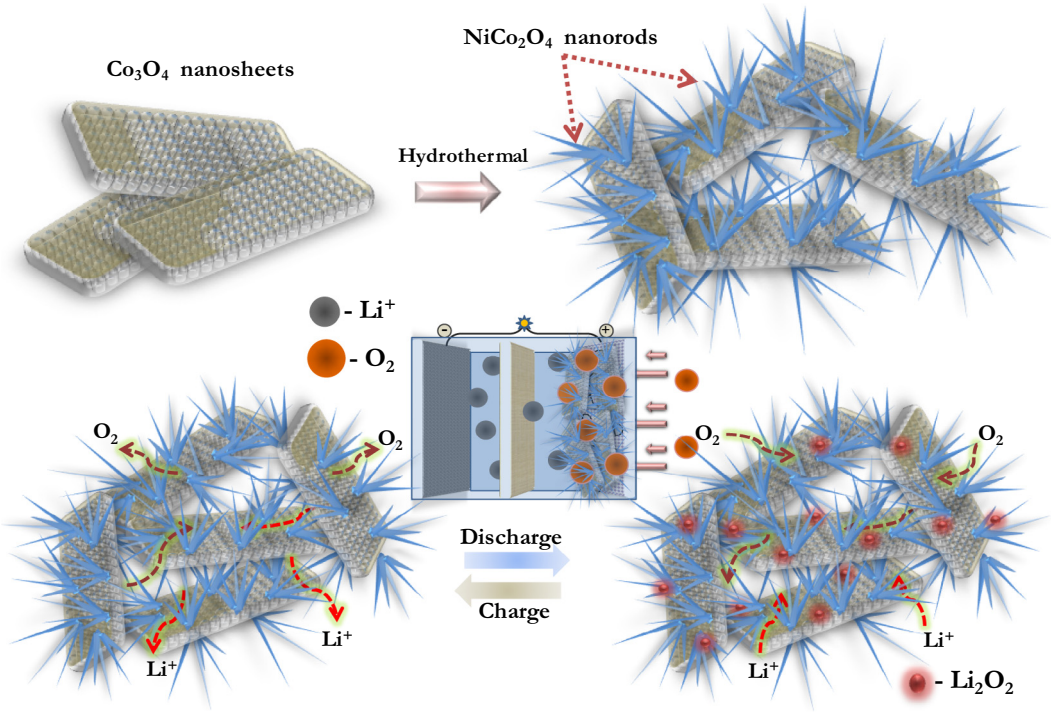

Scheme 1. Formation of 3D structured $NiCo_2O_4$@Co_3O_4 hybrids.

2.3. Electrode preparation and electrochemical characterization

2.3.1. Rotating ring disk electrode (RRDE) ORR and OER

For the ORR and OER studies, the 3D Co-NC was mixed with carbon powder (Cabot Vulcan carbon XC-72) at a 30:70 wt.% to ensure a sufficient electrical conductivity. Ten milligrams of the above mixture was dispersed ultrasonically in 150 μL of a diluted Nafion alcohol solution (5 wt%) dissolved in isopropyl alcohol (IPA). About 13.5 μL of the above suspension was drop-cast onto a 5.61-mm-diameter of glassy carbon electrode [the area of outer Pt ring is 0.2356 cm^2 (outer disc: 8.5 mm, inner disc: 6.5 mm)] as an RRDE electrode (Pine research instrumentation). The Co_3O_4-NS and a 20 wt.% Pt/C electrode (Premetek Co.) were also studied for comparison. Cyclic voltammetry (CV) and linear sweep voltammetry (LSV) were recorded using a computerized potentiostatic instrument (model CHI700C). This three-electrode setup in a glass cell consisted of the RRDE as the working electrode, the Pt wire as the counter electrode, and Hg/HgO (1 M NaOH electrolyte) as a reference electrode immersed in O_2-saturated 0.1 M KOH as an electrolyte solution at ambient temperature conditions. For the CV measurements, the scan rate and disk rotation rate were fixed to 5 mV s^{-1} and 1600 rpm, respectively. For each analysis (ORR, OER and durability test), we used the same mass loading for all the electrodes (40 μg cm^{-2}).

2.3.2. Li–O_2 battery

For the formulation of the O_2 electrode, the catalyst and KB (1:2 ratio) were mixed with a teflonized acetylene black (TAB-2) binder in isopropanol, formed into a pellet, and then pressed onto a Ni mesh current collector. Further, the electrodes were dried in vacuum at 100 °C for 12 h and subsequently employed as a cathode for a Li–O_2 battery. The catalytic performance of the catalyst was evaluated in a Swagelok™-type Li–O_2 cell containing the 1 M lithium bis(trifluoromethane)sulfonimide (LiTFSI) in tetraethylene glycol dimethyl ether (TEGDME) electrolyte, and metallic lithium was used as the anode. The CV traces were recorded within the range of 1.5–4.7 V *vs.* Li using a Won-A-Tech (WBCS 3000, Korea) battery tester. However, the galvanostatic charge/discharge cycling of the cells was recorded in the potential window of 2–4.3 V *vs.* Li at different current densities (0.1–0.4 mA cm^{-2}) using a BTS 2004 (JAPAN) battery tester at a room temperature.

3. Results and discussion

3.1. Physical studies

The crystalline phases of the as-prepared Co-NC and Co_3O_4-NS were confirmed by powder XRD measurements (Fig. 1a). The obtained XRD patterns can be indexed according to the (311), (511), (440), (400), and (220) reflections of cubic Co_3O_4 (ICDD No. 01-076-1802) without any secondary phases [37,38]. This clearly indicates no changes in the Co_3O_4-NS crystal structure after $NiCo_2O_4$-NR growth, and the crystal pattern of $NiCo_2O_4$ perfectly matched that of spinel Co_3O_4.

The composition and structure of the Co-NC and Co_3O_4-NS were further confirmed by Raman analysis, as shown in Fig. 1b. The five Raman active vibration modes of the Co_3O_4-NS, *i.e.*, A_{1g} (~681 cm^{-1}), $3F_{2g}$ (~609, ~520, and ~199 cm^{-1}), and E_g (~477 cm^{-1}), and its position correspond to the cubic spinel structure and are consistent with the literature [39]. The insertion of nickel into the spinel lattice significantly alters the Raman peaks and substantially shifts them to higher frequencies. The most significant shift to higher frequencies is observed for the A_{1g} reflection from ~669 to ~658 cm^{-1}, which is induced at the octahedral cation sites by the substitution of cobalt cations with Ni^{2+}. The

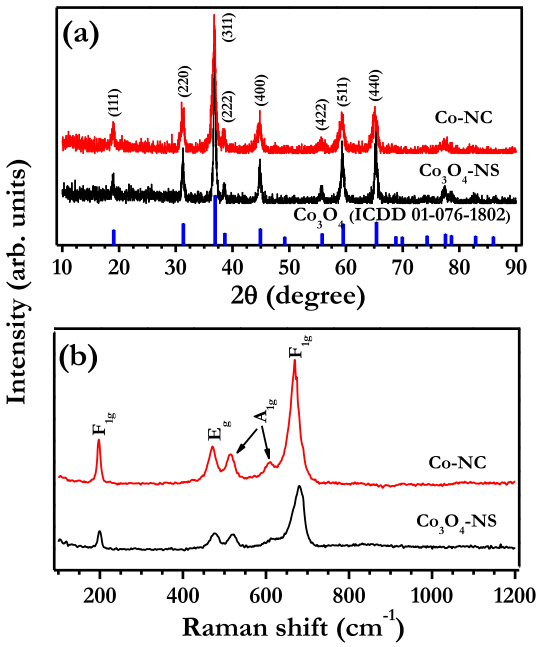

Fig. 1. (a) XRD patterns and (b) Raman spectra of the as-synthesized Co_3O_4-NS (black line) and Co-NC (red line).

F_{2g} and E_g bands are also displaced to higher frequencies to a lesser extent by ~7 and ~6 cm^{-1}, respectively. These minor deviations in the peak positions result from the fact that symmetric stretching of the Co–O vibration mode involves both tetrahedral and octahedral sites, in which only the octahedral site is affected by nickel ion substitution [40–42]. The porous nature of the Co_3O_4-NS and Co-NC was analyzed by N_2 adsorption–desorption isotherms and is presented in Fig. S1 and Table S1. The major uptake of N_2 occurs at a relatively high pressure ($P/P_0 > 0.7$), which is a fingerprint of a type-IV isotherm with a mesoporous structure.

The morphological features of Co-NC were analyzed by FE-SEM and HR-TEM studies and are shown in Fig. 2. Fig. 2a and b shows FE-SEM images of Co-NC, which is composed of a regular bundle such as the $NiCo_2O_4$ nanoflowers grown along the surface, and nanorods are grown at the edge sites of the Co_3O_4-NS (Fig. S2). Most of the nanorods are created as building blocks and connected with Co_3O_4-NS into a 3D structure. The lengths of the $NiCo_2O_4$ nanorods vary in the range of ~0.7–1.5 μm, as clearly shown in Fig. 2c. The HR-TEM images (Fig. 2d) show that the lattice fringes of the shell, ~0.236, ~0.209, and ~0.154 nm, correspond to the (311), (400), and (511) planes of spinel-structured $NiCo_2O_4$. Fig. 2e shows a selected-area electron diffraction (SAED) pattern of Co-NC and consists of well-defined diffraction rings, indicating the polycrystalline nature of the crystal. This can be readily indexed according to the (444), (224), (400), and (222) planes of the cubic $NiCo_2O_4$ phase, which is consistent with the XRD results. The energy dispersive spectroscopy maps of Co-NC clearly show an uniform distribution of Co (red), Ni (green), and O (yellow) elements (Fig. 2f). In order to further confirm the chemical composition of Co-NC, XPS studies were performed, and the results are presented in Fig. S3. The survey spectrum clearly suggests the presence of different elements such as Ni, Co, and O, which corroborates the earlier studies.

3.2. Electrochemical studies

3.2.1. Catalytic activity in aqueous media

The inexpensive Co-NC composite has been used as bifunctional electrocatalyst for the air electrode in Li–O_2 battery applications.

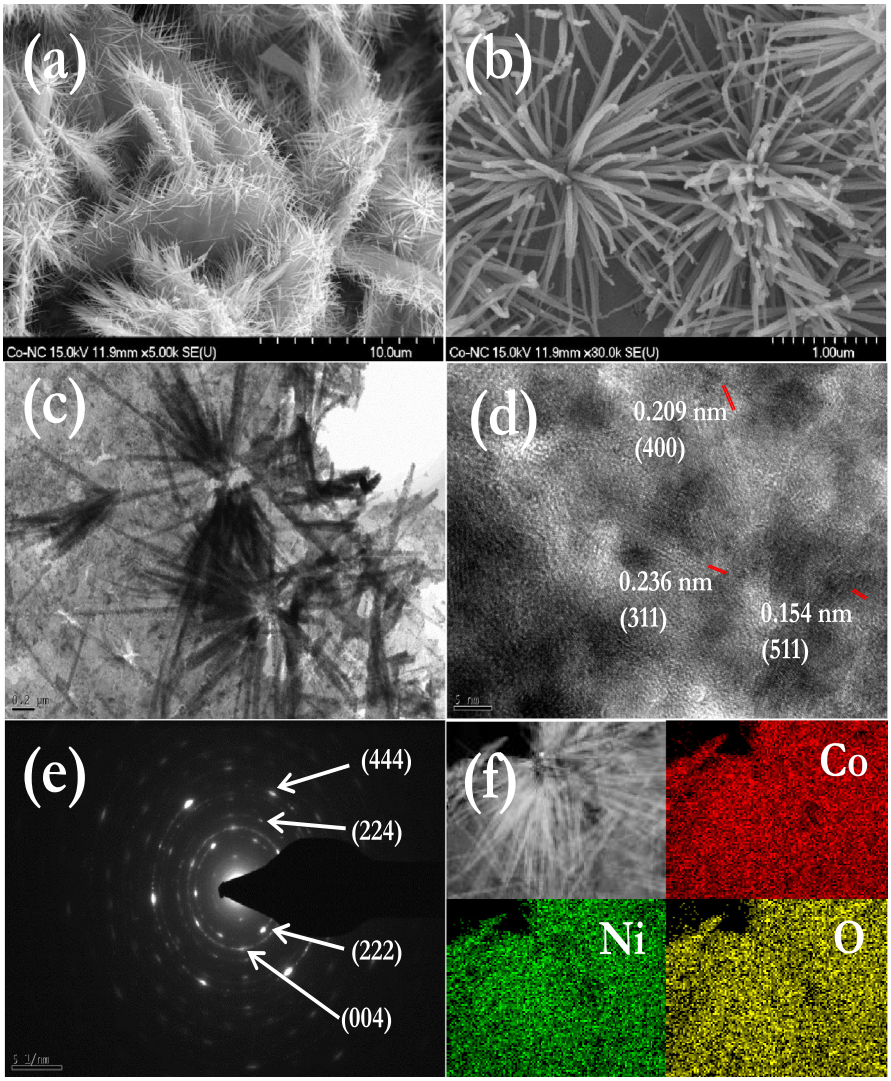

Fig. 2. (a, b) Scanning electron microscope (SEM) images, (c, d) high-resolution transmission electron microscope (HR-TEM) images, (e) SAED pattern, and (f) EDS map of Co-NC.

Initially, the electrochemical activities of the Co_3O_4-NS and Co-NC are examined in an O_2-saturated 0.1 M KOH solution *vs.* Hg/HgO *via* CV and LSV analyses at a rotation speed of 1600 rpm. For comparison, a commercial Pt/C (20 wt%) electrode was also used in the RRDE technique. Fig. 3a shows the CV profiles recorded in the range of −0.8 to 0.3 V *vs.* Hg/HgO at a scan rate of 5 mV s^{-1}, which display a well-defined peak at −0.23 V for the Co_3O_4-NS. A positively shifted cathodic peak is observed for Co-NC with a higher reaction peak current density of −0.22 mA cm^{-2}. This clearly suggests enhanced synergetic effects with better electronic movement in Co-NC. Specifically, the porous structure of Co-NC can accommodate more electrolytes and facilitate efficient OH^- transport to active sites for improved ORR catalytic activity. The ORR and OER activities of the catalysts are studied using the LSV method at a scan rate of 5 mV s^{-1} with a rotation rate of 1600 rpm. The ORR activity can be accessed directly from the onset potential from the LSV curves and the half-wave potential of the catalyst recorded between −0.8 and 0.3 V *vs.* Hg/HgO, as presented in Fig. 3b and Table 1. The onset potentials of the Co_3O_4-NS, Co-NC, and the Pt/C electrode are −0.13, −0.091, and 0.062 V, respectively. Apparently, the onset potential of the Co_3O_4-NS is more negative compared to that of Co-NC and the Pt/C electrode. The observed limited diffusion current for Co-NC is ~0.106 mA higher than that of the Co_3O_4-NS catalyst.

Fig. 3c shows the ORR catalytic kinetics examined using Tafel plots in the low-overpotential region according to the Koutecky–Levich method. The linear Tafel slope of Co-NC is about 72 mV dec^{-1}, which is smaller than that of the Co_3O_4-NS-based catalyst (79 mV dec^{-1}). A smaller Tafel slope and higher catalytic current density indicate a faster increase in the ORR kinetics with decreasing potential. This ORR activity is very close to that of the Pt/C-based system (68 mV dec^{-1}). To validate the ORR catalytic pathway from the peroxide species (OH_2^-), the number of electrons transferred (n) during the ORR was calculated from the ring and disk currents (Fig. S5) according to the following equations [43,44]:

$$OH_2^- = 200\frac{\frac{I_r}{N}}{I_d + \frac{I_r}{N}} \quad (1)$$

$$n = 4\frac{I_d}{I_d + \frac{I_r}{N}} \quad (2)$$

where I_d and I_r are the disk current and ring current, respectively. N is the current collection efficiency in the RRDE (N = 0.37). The measured percentage of HO_2^- formation in Co-NC (3–13%) is lower than that of the Co_3O_4-NS (6–20%) within the potential range of −0.8 to −0.2 V. The number of electrons transferred for Co-NC is 3.77–3.93 higher than that of the Co_3O_4-NS (3.66–3.87), suggesting that the

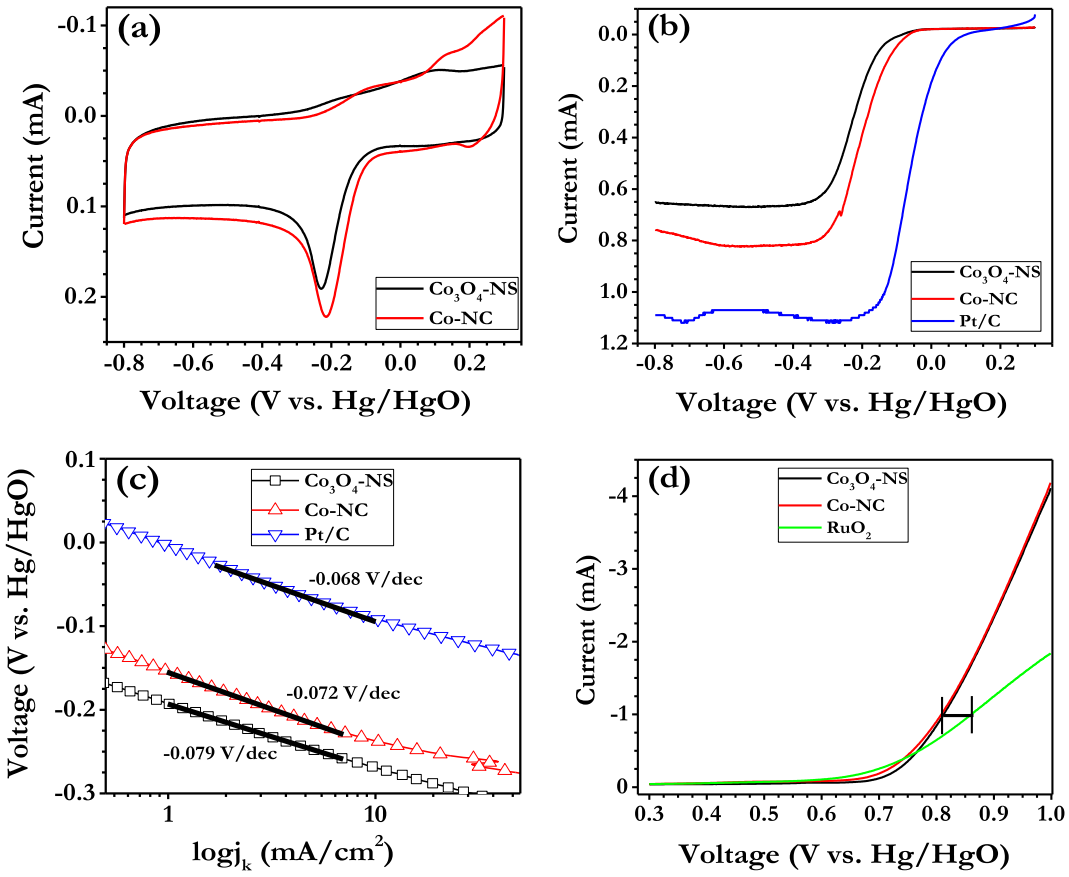

Fig. 3. Comparison of the (a) cyclic voltammograms, (b) ORRs, (c) Tafel plots, and (d) OERs of the Co_3O_4-NS (black line) with Co-NC (red line), Pt/C (blue line), and RuO_2 (green line) catalysts in an O_2-saturated 0.1 M KOH solution at a scan rate of 5 mV s^{-1}.

Table 1
Comparison of the CV, ORR, OER and Tafel plot data of the Co_3O_4 NS, Co-NC, commercial Pt/C and RuO_2 catalysts.

Samples	CV		ORR		OER		Tafel slope
	Peak potential (V)	Peak current (mA)	Onset potential (V)	Apex current (mA)	Apex current (mA)	Half -wave potential (V)	Slope (V/dec)
Pt/C	–	–	0.062	1.09	–	–	−0.068
Co-NC	−0.21	0.222	−0.091	0.758	−4.18	0.809	−0.072
Co_3O_4 NS	−0.23	0.191	−0.13	0.652	−4.11	0.812	−0.079
RuO_2	–	–	–	–	−1.84	0.861	–

ORR catalyzed by our Co-NC proceeds with a quasi-4-electron reduction. To understand the OER behavior of the catalyst, studies are carried out at 0.3–1 V *vs.* Hg/HgO, as shown in Fig. 3d. The OER half-wave potentials observed at the apex of current are 1 mA cm^{-2} for the Co_3O_4-NS, Co-NC, and Pt/C electrode (20 wt%) samples are 0.813, 0.809, and 0.91 V, respectively. Co-NC showed a 92 mV positively shifted OER activity compared to the Pt/C electrode. In addition, the corresponding Tafel plots are constructed on the basis of the LSV curves (Fig. S6). The coupling between $NiCo_2O_4$ and the Co_3O_4-NS is beneficial, resulting in an improved catalytic pathway toward the ORR/OER reaction kinetics. The substitution of lower valence Ni^{2+} ions at the spinel Co_3O_4 octahedral sites creates oxygen-deficient sites and enlarges its specific surface area at the microscopic level. The enhanced catalytic activity of Co-NC results from a high conductivity and effective charge transfer at the electrode/electrolyte interface. These results suggest that Co-NC can serve as an efficient bifunctional electrocatalyst for the ORR and OER processes in an aqueous electrolyte.

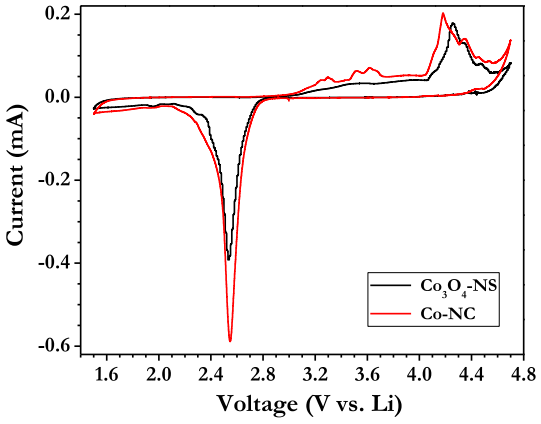

Fig. 4. Comparison of the cyclic voltammograms of the Co_3O_4-NS and Co-NC catalysts in Li–O_2 cells at a sweep rate of 0.1 mV s^{-1}.

3.2.2. Li–O_2 battery

Electro-catalytic activities of the Co-NC and Co_3O_4-NS electrodes were investigated by CV in an oxygen-saturated 1 M LiTFSI/TEGDME solution between 1.5 and 4.7 V *vs.* Li at a sweep rate of 0.1 mV s^{-1} and given in Fig. 4. Oxygen reduction was observed at 2.92 and 2.82 V *vs.* Li for the Co-NC and Co_3O_4-NS-based electrodes, respectively. Moreover, a very strong cathodic peak was observed around 2.54 V *vs.* Li for both electrodes (Table 2). However, the peak current (−0.59 mA) of the Co-NC-based electrode is much higher than that of the Co_3O_4-NS (−0.392 mA), which is mainly related to the better conductivity and efficient reduction activity of the former electrode compared to latter. During the subsequent anodic scan, the Co-NC electrode showed two distinguishable peaks at ~3.3 and 3.6 V, which are the oxidation potentials of amorphous and crystalline Li_2O_2, respectively. The oxidation of oxygen-rich amorphous Li_2O_2 takes place in solution, but the crystalline-phase oxidation occurs on the catalyst surface through an intermediate composed of the pre-lithiated catalyst and lithium-deficient $Li_{2-x}O_2$ based on Eq. (5). The oxidation of Li_2CO_3 or electrolyte decomposition was initiated at above 4.3 V *vs.* Li [11,45–47]. The peak current is much more considerable for Co-NC (0.202 mA) compared to the Co_3O_4-NS electrode, which exhibits a weak current response (0.179 mA) with a shifted decomposition potential toward a higher potential of ~4.26 V *vs.* Li. The CV measurement clearly indicates efficient catalytic activity with a lower polarization for the Co-NC electrode, which certainly enhances the energy output and round-trip efficiencies during the reduction and oxidation processes compared to those of the Co_3O_4-NS based electrode in a Li–O_2 battery.

$$O_2 + e^- + Li^+ \rightarrow LiO_2 \quad (3)$$

$$LiO_2 + e^- + Li^+ \leftrightarrow Li_2O_2 \quad (4)$$

$$Li_2O_2 \rightarrow Li_{2-x}O_2 \rightarrow 2 - xLi^+ + 2 - xe^- + O_2 \quad (5)$$

The galvanostatic charge–discharge performance of the Co_3O_4-NS and Co-NC catalysts was determined at 2–4.3 V *vs.* Li at a current density of 0.1 mA cm^{-2} (0.1 A g^{-1}) in a Swagelok-type cell and is shown in Fig. 5. The Li–O_2 cell delivered first discharge capacities of ~4265 and 4386 mA h g^{-1} for the Co_3O_4-NS and Co-NC catalysts, respectively. For comparison, pure KB was also evaluated under the same conditions, but the first discharge capacity of ~3143 mA h g^{-1} is ~29% lower compared to the Co-NC-based cell (Fig. S7). The over-potentials (the difference between the charge and discharge voltages at the specific capacity) for the Co_3O_4-NS and Co-NC catalysts are 1.378 and 1.078 V, respectively. In the 3rd cycle, the capacity retention (with respect to the first discharge) and round-trip efficiency are ~81 and 99% for the Co-NC-based cell. Further, these values are much higher than those of the Co_3O_4-NS-based system (~55% and 97%). The non-aqueous-electrolyte-based Li–O_2 battery system consists of Li_2O_2 as the main product, and Li_2CO_3 can be formed through side reactions during cycling. Therefore, the slow increase in the overpotential may be caused by the accumulation of residual Li_2O_2 and Li_2CO_3 on the surface of the active sites and/or partial decomposition upon charging. This would certainly decrease the conductivity of the electrode and eventually worsen the reversibility of the Co_3O_4-NS-based Li–O_2 battery.

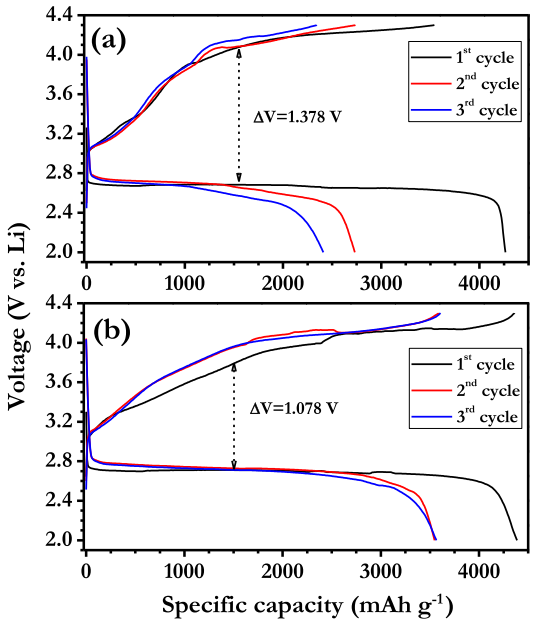

Fig. 5. The charge/discharge patterns of the (a) Co_3O_4-NS- and (b) Co-NC-based catalysts in Li–O_2 cells at 0.1 mA cm^{-2} (or 0.1 A g^{-1}).

Fig. 6a shows a comparison of the first charge–discharge curve of Co-NC-based Li–air batteries at different current densities ranging from 0.1 to 0.4 mA cm^{-2} (0.1–0.4 A g^{-1}). When the current density decreases from 0.4 to 0.1 mA cm^{-2}, the depth discharge capacity increases from 1233 to 4386 mA h g^{-1}, and the round-trip efficiency changes from 62.5% to 99.4%. In addition, the voltage gap between the charge and discharge plateaus tends to decrease, suggesting a good rate capability. The cycleabilities of the Co-NC and Co_3O_4-NS catalysts based Li-O_2 cells were investigated at a controlled specific capacity of 500 mA h g^{-1} and a current density of 0.1 mA cm^{-2} and are shown in Fig. 6 and S8. The cycling performance of the cell with the Co_3O_4-NS electrode is much poorer than that of Co-NC, and the initial terminal discharge voltage is 2.63 V *vs.* Li. After 35 cycles, the overpotential of each cycle increased very slowly, implying that more and more energy is required for the charging and discharging processes. This increased overpotential eventually triggers the drastic polarization of the cell followed by a serious cyclic degradation as well. The discharge capacity decreases to less than 500 mA h g^{-1} after the 40th and 50th cycles and remains only ~256 and 41 mA h g^{-1}, respectively. However, Co-NC shows the lowest overpotential and maintains a great round-trip efficiency up to 60 cycles with a slight increase in the polarization (Fig. S7b). The morphologies of the discharge products and the reversibility of the formation and decomposition were analyzed using an XRD and FE-SEM and are given in Fig. S9. The XRD pattern of the discharge product consists of both Li_2O_2 and HLiO or LiOH along with $NiCo_2O_4$, which is clearly evident, and the corresponding reference patterns are also given. The LiOH is one

Table 2
The ORR and OER data from the CV curve of the Co_3O_4 NS with Co-NC in a 1 M LiTFSI–TEGDME electrolyte.

Samples	ORR		OER	
	Peak potential (V)	Peak current (mA)	Peak potential (V)	Peak current (mA)
Co-NC	2.54	−0.590	4.18	0.179
Co_3O_4 NS	2.54	−0.392	4.26	0.202

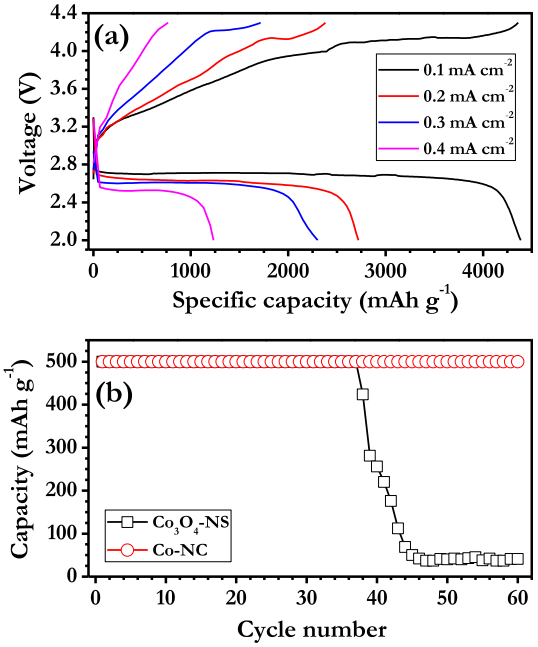

Fig. 6. (a) Rate performance of a Li–O_2 cell with a Co-NC catalyst at different current densities. (b) The limited capacity cycling performance of the Co_3O_4-NS and Co-NC catalysts in Li–O_2 cells at a current rate of 0.1 mA cm^{-2} (0.1 A g^{-1}).

of discharge products, when the trace amount of moisture is present in non-aqueous electrolyte and/or formed along with the Li_2O_2. These products are often enhancing the specific capacity and cycling stability of Li-O_2 cell [48]. Apparently, the 3D architecture has dissociated, and a leaf-like rod morphology appears after the discharge process. Upon charging, the again started to disappear, probably removed from the surface.

The porous structure of Co-NC favors the uniform distribution of discharge products during discharge and ensures complete decomposition in the subsequent charge process. Meanwhile, the doping of Ni^{2+} ions creates an oxygen-deficient crystal structure in the spinel Co_3O_4, and the integrated morphology of the 1D $NiCo_2O_4$-NR over the Co_3O_4-NS also promotes the decomposition and formation of Li_2O_2 in Co-NC. Nevertheless, a slightly elevated polarization is noted upon cycling, but better electrochemical properties on the surface are observed, leading to an improvement in the round-trip efficiency and excellent long-term stability that is cost-effective compared with noble-metal catalysts. This study clearly indicates that Co-NC could be used as promising bifunctional catalyst for the development of high-performance Li–air battery applications.

4. Conclusion

In this work, we have successfully designed 1D/2D structured Co-NC hybrids, *i.e.*, nanorods grown over nanosheets, prepared by a two-step hydrothermal method. The porous structure of the Co-NC hybrids facilitates O_2 and electrolyte transport in the inner electrode, and its superior catalytic activity efficiently decomposes the discharge products. Electrocatalytic evaluations in both aqueous and nonaqueous electrolytes reveal that the prepared Co-NC hybrids possess enhanced electrochemical performance with a reduced overpotential compared with the Co_3O_4-NS catalyst. The Co-NC-hybrid-catalyzed Li–O_2 battery delivers a specific capacity at the depth discharge condition of 4386 mA h g^{-1} at 0.1 mA cm^{-2} and demonstrates 60 stable cycles at the limited capacity of 500 mA h g^{-1}. In conclusion, the substitution of low-valence Ni^{2+} ions creates oxygen-deficient sites, and the integrated porous structure enhances the catalytic activity of the Co-NC hybrids, leading to an improvement in the round-trip efficiency and an excellent long-term stability for Li-O_2 batteries. Also, this catalyst could be used as efficient catalyst for water splitting and metal-air batteries such as Zn-O_2 and Li-O_2 batteries (aq.) as well.

Acknowledgment

This work was supported by the Industrial Technology Innovation Program of KEIT (10053725, Development of manufacturing technology for layered high capacity (≥ 210 mA h g^{-1}) cathode material as for high-power output LIB through recycling) funded by the Ministry of Trade, Industry & Energy (MI, Korea).

Appendix A. Supplementary material

Supplementary data associated with this article can be found, in the online version, at http://dx.doi.org/10.1016/j.jcat.2017.03.015.

References

[1] J. Christensen, P. Albertus, R.S. Sanchez-Carrera, T. Lohmann, B. Kozinsky, R. Liedtke, J. Ahmed, A. Kojic, A critical review of Li/air batteries, J. Electrochem. Soc. 159 (2011) R1–R30.
[2] G. Girishkumar, B. McCloskey, A.C. Luntz, S. Swanson, W. Wilcke, Lithium–air battery: promise and challenges, J. Phys. Chem. Lett. 1 (2010) 2193–2203.
[3] M. Park, H. Sun, H. Lee, J. Lee, J. Cho, Lithium-air batteries: survey on the current status and perspectives towards automotive applications from a battery industry standpoint, Adv. Energy Mater. 2 (2012) 780–800.
[4] L. Grande, E. Paillard, J. Hassoun, J.-B. Park, Y.-J. Lee, Y.-K. Sun, S. Passerini, B. Scrosati, The lithium/air battery: still an emerging system or a practical reality?, Adv Mater. 27 (2015) 784–800.
[5] P.G. Bruce, S.A. Freunberger, L.J. Hardwick, J.-M. Tarascon, Li-O_2 and Li-S batteries with high energy storage, Nat. Mater. 11 (2012) 19–29.
[6] R. Black, B. Adams, L.F. Nazar, Non-aqueous and hybrid Li-O_2 batteries, Adv. Energy Mater. 2 (2012) 801–815.
[7] B.D. McCloskey, D.S. Bethune, R.M. Shelby, G. Girishkumar, A.C. Luntz, Solvents' critical role in nonaqueous lithium-oxygen battery electrochemistry, J. Phys. Chem. Lett. 2 (2011) 1161–1166.
[8] K.M. Abraham, Z. Jiang, A polymer electrolyte-based rechargeable lithium/oxygen battery, J. Electrochem. Soc. 143 (1996) 1–5.
[9] R. Black, J.-H. Lee, B. Adams, C.A. Mims, L.F. Nazar, The role of catalysts and peroxide oxidation in lithium-oxygen batteries, Angew. Chem. 125 (2013) 410–414.
[10] M. Shao, Q. Chang, J.-P. Dodelet, R. Chenitz, Recent advances in electrocatalysts for oxygen reduction reaction, Chem. Rev. 116 (2016) 3594–3657.
[11] K.P.C. Yao, M. Risch, S.Y. Sayed, Y.-L. Lee, J.R. Harding, A. Grimaud, N. Pour, Z. Xu, J. Zhou, A. Mansour, F. Barde, Y. Shao-Horn, Solid-state activation of Li_2O_2 oxidation kinetics and implications for Li-O_2 batteries, Energy Environ. Sci. 8 (2015) 2417–2426.
[12] A. Débart, J. Bao, G. Armstrong, P.G. Bruce, An O_2 cathode for rechargeable lithium batteries: the effect of a catalyst, J. Power Sources 174 (2007) 1177–1182.
[13] J. Jung, K. Song, Y. Bae, S.-I. Choi, M. Park, E. Cho, K. Kang, Y.-M. Kang, Achieving outstanding Li^+-ORR and -OER activities via edge- and corner-embedded bimetallic nanocubes for rechargeable Li-O_2 batteries, Nano Energy 18 (2015) 71–80.
[14] S.-I. Choi, S. Xie, M. Shao, J.H. Odell, N. Lu, H.-C. Peng, L. Protsailo, S. Guerrero, J. Park, X. Xia, J. Wang, M.J. Kim, Y. Xia, Synthesis and characterization of 9 nm Pt–Ni octahedra with a record HIGH activity of 3.3 A/mg Pt for the oxygen reduction reaction, Nano Lett. 13 (2013) 3420–3425.
[15] J. Kim, Y. Lee, S. Sun, Structurally ordered FePt nanoparticles and their enhanced catalysis for oxygen reduction reaction, J. Am. Chem. Soc. 132 (2010) 4996–4997.
[16] H. Yang, J. Zhang, K. Sun, S. Zou, J. Fang, Enhancing by weakening: electrooxidation of methanol on Pt_3Co and Pt nanocubes, Angew. Chem. Int. Ed. 49 (2010) 6848–6851.
[17] Y.-C. Lu, Z. Xu, H.A. Gasteiger, S. Chen, K. Hamad-Schifferli, Y. Shao-Horn, Platinum–gold nanoparticles: a highly active bifunctional electrocatalyst for rechargeable lithium–air batteries, J. Am. Chem. Soc. 132 (2010) 12170–12171.
[18] P. Sennu, M. Christy, V. Aravindan, Y.-G. Lee, K.S. Nahm, Y.-S. Lee, Two-dimensional mesoporous cobalt sulfide nanosheets as a superior anode for a Li-Ion battery and a bifunctional electrocatalyst for the Li–O_2 system, Chem. Mater. 27 (2015) 5726–5735.
[19] G. Zhao, Z. Xu, K. Sun, Hierarchical porous Co_3O_4 films as cathode catalysts of rechargeable Li-O_2 batteries, J. Mater. Chem. A 1 (2013) 12862–12867.

[20] Y. Kang, C.B. Murray, Synthesis and electrocatalytic properties of cubic Mn–Pt nanocrystals (Nanocubes), J. Am. Chem. Soc. 132 (2010) 7568–7569.
[21] A. Zahoor, M. Christy, H. Jang, K.S. Nahm, Y.S. Lee, Increasing the reversibility of Li–O_2 batteries with caterpillar structured α–MnO_2/N–GNF bifunctional electrocatalysts, Electrochim. Acta 157 (2015) 299–306.
[22] A. Débart, A.J. Paterson, J. Bao, P.G. Bruce, α-MnO_2 nanowires: A catalyst for the O_2 electrode in rechargeable lithium batteries, Angew. Chem. Int. Ed. 47 (2008) 4521–4524.
[23] A. Gupta, W.D. Chemelewski, C. Buddie Mullins, J.B. Goodenough, High-rate oxygen evolution reaction on Al-doped $LiNiO_2$, Adv. Mater. 27 (2015) 6063–6067.
[24] Y. Li, L. Zou, J. Li, K. Guo, X. Dong, X. Li, X. Xue, H. Zhang, H. Yang, Synthesis of ordered mesoporous $NiCo_2O_4$ via hard template and its application as bifunctional electrocatalyst for Li-O_2 batteries, Electrochim. Acta 129 (2014) 14–20.
[25] Z. Wu, Y. Zhu, X. Ji, $NiCo_2O_4$-based materials for electrochemical supercapacitors, J. Mater. Chem. A 2 (2014) 14759–14772.
[26] Y. Li, P. Hasin, Y. Wu, $Ni_xCo_{3-x}O_4$ nanowire arrays for electrocatalytic oxygen evolution, Adv. Mater. 22 (2010) 1926–1929.
[27] X. Wang, W.S. Liu, X. Lu, P.S. Lee, Dodecyl sulfate-induced fast faradic process in nickel cobalt oxide-reduced graphite oxide composite material and its application for asymmetric supercapacitor device, J. Mater. Chem. 22 (2012) 23114–23119.
[28] B. Wu, H. Zhang, W. Zhou, M. Wang, X. Li, H. Zhang, Carbon-free CoO mesoporous nanowire array cathode for high-performance aprotic Li–O_2 batteries, ACS Appl. Mater. Interfaces. 7 (2015) 23182–23189.
[29] H. Lee, Y.-J. Kim, D.J. Lee, J. Song, Y.M. Lee, H.-T. Kim, J.-K. Park, Directly grown Co_3O_4 nanowire arrays on Ni-foam: structural effects of carbon-free and binder-free cathodes for lithium-oxygen batteries, J. Mater. Chem. A 2 (2014) 11891–11898.
[30] Y. Cui, Z. Wen, Y. Liu, A free-standing-type design for cathodes of rechargeable Li-O_2 batteries, Energy Environ. Sci. 4 (2011) 4727–4734.
[31] J.-J. Xu, Z.-L. Wang, D. Xu, F.-Z. Meng, X.-B. Zhang, 3D ordered macroporous $LaFeO_3$ as efficient electrocatalyst for Li-O_2 batteries with enhanced rate capability and cyclic performance, Energy Environ. Sci. 7 (2014) 2213–2219.
[32] D. Kundu, R. Black, E.J. Berg, L.F. Nazar, A highly active nanostructured metallic oxide cathode for aprotic Li-O_2 batteries, Energy Environ. Sci. 8 (2015) 1292–1298.
[33] A. Riaz, K.-N. Jung, W. Chang, S.-B. Lee, T.-H. Lim, S.-J. Park, R.-H. Song, S. Yoon, K.-H. Shin, J.-W. Lee, Carbon-free cobalt oxide cathodes with tunable nanoarchitectures for rechargeable lithium-oxygen batteries, Chem. Commun. 49 (2013) 5984–5986.
[34] Y. Cui, Z. Wen, X. Liang, Y. Lu, J. Jin, M. Wu, X. Wu, A tubular polypyrrole based air electrode with improved O_2 diffusivity for Li-O_2 batteries, Energy Environ. Sci. 5 (2012) 7893–7897.
[35] A. Zahoor, H.S. Jang, J.S. Jeong, M. Christy, Y.J. Hwang, K.S. Nahm, A comparative study of nanostructured α and δ MnO_2 for lithium oxygen battery application, RSC Adv. 4 (2014) 8973–8977.
[36] D. Zhao, J.-L. Shui, L.R. Grabstanowicz, C. Chen, S.M. Commet, T. Xu, J. Lu, D.-J. Liu, Highly efficient non-precious metal electrocatalysts prepared from one-pot synthesized zeolitic imidazolate frameworks, Adv. Mater. 26 (2014) 1093–1097.
[37] P. Sennu, V. Aravindan, Y.-S. Lee, High energy asymmetric supercapacitor with 1D/2D structured $NiCo_2O_4$@Co_3O_4 and jackfruit derived high surface area porous carbon, J. Power Sources 306 (2016) 248–257.
[38] P. Sennu, H.S. Kim, J.Y. An, V. Aravindan, Y.-S. Lee, Synthesis of 2D/2D structured mesoporous Co_3O_4 nanosheet/N-doped reduced graphene oxide composites as a highly stable negative electrode for lithium battery applications, Chem. – Asian J. 10 (2015) 1776–1783.
[39] Z.-Q. Liu, K. Xiao, Q.-Z. Xu, N. Li, Y.-Z. Su, H.-J. Wang, S. Chen, Fabrication of hierarchical flower-like super-structures consisting of porous $NiCo_2O_4$ nanosheets and their electrochemical and magnetic properties, RSC Adv. 3 (2013) 4372–4380.
[40] M.N. Iliev, P. Silwal, B. Loukya, R. Datta, D.H. Kim, N.D. Todorov, N. Pachauri, A. Gupta, Raman studies of cation distribution and thermal stability of epitaxial spinel $NiCo_2O_4$ films, J. Appl. Phys. 114 (2013) 033514.
[41] E. Umeshbabu, G. Rajeshkhanna, P. Justin, G.R. Rao, Magnetic, optical and electrocatalytic properties of urchin and sheaf-like $NiCo_2O_4$ nanostructures, Mater. Chem. Phys. 165 (2015) 235–244.
[42] C.-W. Tang, C.-B. Wang, S.-H. Chien, Characterization of cobalt oxides studied by FT-IR, Raman, TPR and TG-MS, Thermochim. Acta 473 (2008) 68–73.
[43] Y. Liang, Y. Li, H. Wang, J. Zhou, J. Wang, T. Regier, H. Dai, Co_3O_4 nanocrystals on graphene as a synergistic catalyst for oxygen reduction reaction, Nat. Mater. 10 (2011) 780–786.
[44] P. Li, R. Ma, Y. Zhou, Y. Chen, Z. Zhou, G. Liu, Q. Liu, G. Peng, Z. Liang, J. Wang, In situ growth of spinel $CoFe_2O_4$ nanoparticles on rod-like ordered mesoporous carbon for bifunctional electrocatalysis of both oxygen reduction and oxygen evolution, J. Mater. Chem. A 3 (2015) 15598–15606.
[45] C.O. Laoire, S. Mukerjee, K.M. Abraham, E.J. Plichta, M.A. Hendrickson, Influence of nonaqueous solvents on the electrochemistry of oxygen in the rechargeable lithium–air battery, J. Phys. Chem. C 114 (2010) 9178–9186.
[46] J. Yi, X. Liu, S. Guo, K. Zhu, H. Xue, H. Zhou, Novel stable gel polymer electrolyte: toward a high safety and long life li–air battery, ACS Appl. Mater. Interfaces. 7 (2015) 23798–23804.
[47] Y. Zhu, S. Liu, C. Jin, S. Bie, R. Yang, J. Wu, MnO_x decorated CeO_2 nanorods as cathode catalyst for rechargeable lithium-air batteries, J. Mater. Chem. A 3 (2015) 13563–13567.
[48] J. Lu, L. Li, J.-B. Park, Y.-K. Sun, F. Wu, K. Amine, Aprotic and aqueous Li–O_2 batteries, Chem. Rev. 114 (2014) 5611–5640.